International Journal of Impact Engineering 144 (2020) 103664

Contents lists available at ScienceDirect

International Journal of Impact Engineering

journal homepage: www.elsevier.com/locate/ijimpeng

Effect of target velocity on damage patterns in hypervelocity glancing collisions

A. Dorogoy[a], D. Rittel[a], D. Weihs[b,*]

[a] Faculty of Mechanical Engineering, Technion, 32000, Haifa, Israel
[b] Faculty of Aerospace Engineering, Technion, 32000, Haifa, Israel

ARTICLE INFO

Keywords:
Oblique collision
Normal collision
Hypervelocity impact
Holes
Craters

ABSTRACT

The collisions of space debris, whether human-origin or natural, and spacecraft are essentially hypervelocity impacts. Such collisions pose a serious threat to satellites and spacecraft. While multiple studies, both theoretical and experimental, have dealt with such collisions, none has thoroughly considered the effect of the target's motion during penetration. This results in a different type of collision, beyond normal or oblique penetration, referred to as glancing collision in this work.

This paper studies numerically the effects of such glancing collisions, in which the speeds of both participants are of the same order of magnitude, and not collinear. As an example a simulation of a collision between a projectile moving at 2-10 km/s and a finite target plate moving at 10 km/s laterally, both made of 6061-T6 alloy, also compared to experimental data. The resulting damage is compared to that caused by normal, including comparison with existing experimental data, as well as oblique impact by projectiles at the same velocities where the target is stationary. Two types of projectiles were considered: a sphere and a short cylinder having a hemispherical head. The investigation reveals that glancing collisions result in vastly different craters' shapes and damage patterns with respect to normal collisions. The craters become shallower and more elongated and the damage is not axisymmetric. While the glancing collision is similar to oblique collision for spherical projectiles, it becomes vastly different for elongated non-spherical projectiles.

1. Introduction

Space debris, whether human-origin or natural, is a constant danger to satellites and spacecraft. As the absolute speeds of each of the spacecraft and debris are of the order of several thousand meters per second, any collision can result in penetration of the outer surface (shell) of the spacecraft [1]. Multiple theoretical and experimental studies have dealt with such collisions as detailed in the following paragraphs.

Post-flight surveys of meteoroid and orbital debris impacts on the Space Shuttle Orbiter were conducted in [2] to identify damage and nature of the involved projectiles. This report provides data on an Orbiter over a five-year period and describes in detail the 39 most significant impacts. Of the 39 largest impacts, 29 were caused by orbital debris and 10 were due to meteoroids. None of those impacts did significantly affect the Shuttle's operations or compromised mission objectives.

An extensive analysis of craters caused by the impact of high velocity particles on thick ductile targets, using a micro-particle accelerator, appears in [3]. The aim of that study was to allow an assessment of size, velocity and origin of a projectile from parameters which could be measured on the impact craters formed on aluminum targets. Based on the craters' geometry and the analysis of the remnants, it was shown that the main characteristics of the projectiles can be retrieved.

Projectile/target impact crater systems at impact velocities ranging from 0.56 to 3.99 km/s were examined by electron microscopy [4]. It was observed that the crater geometry begins to change when the projectile velocity is higher than 2 km/s where fragmentation starts and increases with increasing impact velocity. Computer simulations of these impacts were fairly accurate in representing the residual crater shapes/geometries. Numerical extrapolations for hypervelocity impact higher than 5 km/s were also conducted [4].

The development of a new experimental device for launching millimeter size debris at impact velocities between 8 and 12 km/s was the objective of another study [5]. That study presents hypervelocity impacts on different types of targets: single plate, Whipple shield and honeycomb structure, at impact velocities ranging from 7 to 10 km/s.

Much effort has been spent analyzing the effects of both normal and

* Corresponding author.
E-mail address: dweihs@tx.technion.ac.il (D. Weihs).

https://doi.org/10.1016/j.ijimpeng.2020.103664
Received 27 January 2020; Received in revised form 9 July 2020; Accepted 9 July 2020
Available online 15 July 2020
0734-743X/

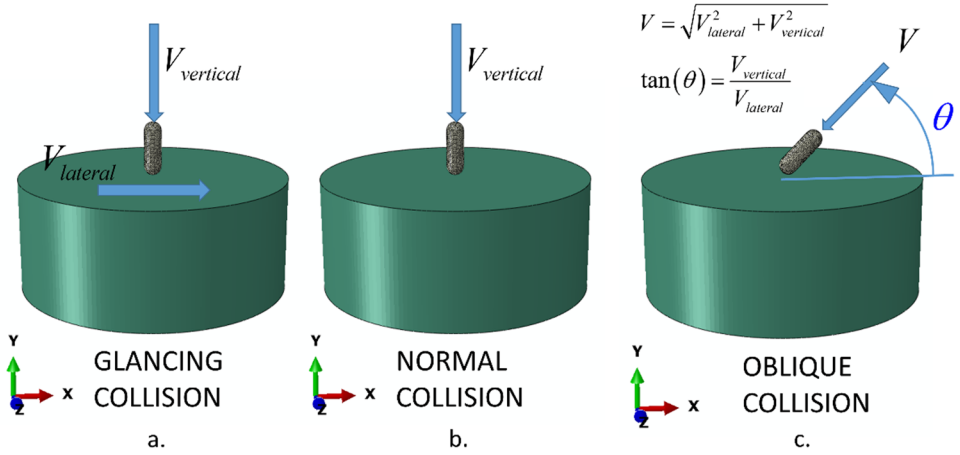

Fig. 1. a. Schematic representation of a. glancing collision, b. normal (perpendicular) collision and c. oblique collision.

oblique impacts. The response of an all-aluminum Whipple shield to hypervelocity impact of 2017-T4 aluminum spheres with diameters ranging from 1.40 to 6.35 mm at impact velocities ranging from 6.94 to 9.89 km/s was tested in [6]. This investigation evaluates the adequacy of the modified Cour-Palais or Christiansen ballistic limit equation [7] and showed that the capability of the shield is better than that predicted by the ballistic limit equations at high impact velocity.

A two-stage light gas gun was used to launch 2017-T4 aluminum alloy spherical projectiles to impact a Whipple shield having a rear aluminum wall [8]. The projectile diameters ranged from 2.51 mm to 5.97 mm and impact velocities ranged from 0.69 km/s to 6.98 km/s. The modes of crater distribution on the rear wall were obtained. It was noticed that, as projectile diameter, impact velocity and shielding spacing increased, the area of crater distribution on the rear aluminum wall increased.

Investigation of hole formation in thin steel target by steel sphere accelerated in a two stage gas gun to velocity range of 2 to 4 km/s and obliquity between 0° and 70° was conducted [9]. A non-dimensional empirical equation for hole formation was determined using simulations, and a few experiments were conducted to validate the predictions. The derived model predictions were satisfactory with error of less than 20% for over 94% of the cases.

Impacts of 2017-T4 aluminum spheres having diameters from 1.40 mm to 19.05 mm on thin 6061-T6 aluminum sheets having sheet-thickness-to-projectile-diameter ratio less than 0.618, were presented and analyzed in [10]. Impact velocities ranged from 1.98 km/s to 9.89 km/s. The results of the analysis of all holes' data was used to develop a description of the hole-formation sequence including the morphology of the lip structure surrounding the hole. This paper was used for comparison with our calculations and the results shown later (and in Appendix C).

Oblique hypervelocity impact testing of multi-sheet specimens was done using a light gas gun capable of launching 2.5-12.7 mm projectiles at velocities of 2-8 km/ s [11]. It was found that obliquely incident projectiles produce ricochet debris that can severely damage panels or instrumentation located on the exterior of a space structure. It was concluded that obliquity effects of high-speed impact must be considered in the design of any structure exposed to the hazardous meteoroid and space debris environment.

Hypervelocity impact of 1 mm diameter aluminum spheres impacting thick glass targets at 5.2 km/s were reported in [12]. The obliquity angle of the projectiles was varied between 0° to 80°. It was found that the measured crater size does not change significantly unless impacts are more than 45° from the normal.

A numerical investigation of the diameter of holes and craters in metallic plates impacted by hypervelocity rods was conducted in [13]. The purpose of this investigation was to relate the hole size (depth, diameter and shape) to the impact velocity and to the material properties of both projectile and plate.

A general collision simulation tool to model the consequences of orbital impacts involving large debris and satellites have been developed [14]. Validation was done by comparing the tool predictions with empirical data from tests on simple plates and Whipple Shields as well as sub-scale spacecraft models. The capability of predicting fragments distributions from plates and ballistic limit was verified.

Hypervelocity collisions (at speeds of thousands of meters per second) are a complex phenomenon, affected by the strength, viscous thermal and shock characteristics of both the impactor and the target.

One major factor was not addressed in all the above-mentioned references. The fact that *both the impactor (debris or meteorite) and target (spacecraft)* are moving at comparable speeds, meaning that a different pattern emerges, which is no longer purely perpendicular or oblique. This was defined earlier as a glancing collision [15] resulting in a non-axisymmetric elongated crater (or hole if the spacecraft skin is penetrated) that, while usually less deep, can involve a different volume of displaced material. It will also produce a different debris cloud from that resulting from either normal or oblique impacts.

Collisions in space will most likely be of the glancing type while laboratory tests which intend to mimic such collisions are using normal or oblique impact, where the target is generally stationary. Fig. 1 illustrates the difference between glancing and oblique/normal collisions.

In this work, we present a numerical parametric study of the effects of such glancing impacts using the commercial ABAQUS numerical code [16]. While no systematic experimental results exist for specifically glancing impacts, we calibrated and validated our calculations by comparing to existing hypervelocity normal impact tests from the literature [10].

To validate our computations, we first compared our numerical results to experimental results of perforation of thin aluminum plates, by normal impact of spherical aluminum projectiles traveling at hypervelocity speed.

We compared to the most relevant experimental results, those of Piekutowski and Poormon [10] with the results appearing in Table C1 in Appendix C . Our results appear in the right column and show agreement within less than 6% to the experiments, except for one outlier having a thicker plate, run 8-3275 . For this run, to ascertain that we are accurately following the experiment, we contacted Dr. Andrew Piekutowski. The comparison, appears below, including a comment by Dr Piekutowski about the changes in measuring the diameter in thicker plates which we also reproduce within less than 10% .

The resulting hole diameters were also compared to the predictions of an empirical model based on a large multiple source data-set [18]. Good agreement was obtained.

Next, we simulated normal impact of a sphere on a thick aluminum plate. Satisfactory agreement was observed for both the crater growth rate, by comparison to Prater [19], and to the final depths of penetration and crater diameters of Nishida et al. [20].

This successful validation paved the way for the investigation of hypervelocity glancing collisions. Simulations of spheres impacting a moving target at 10 km/s normal the spheres trajectories were conducted. The spheres vertical impact velocities were 2 – 10 km/s. The results were compared to normal impact of a stationary target at the same range of impact velocities.

Next, we checked if the damage produced by impacting projectiles in glancing collision is similar/comparable to the damage produced by oblique collision (Fig. 1). Simulations of projectiles impacting normally a 10 km/s moving target at 2-10 km/s were compared to oblique tests at the corresponding angles of inclinations: 11.3°- 45° and velocities (Fig. 1). The effect of two types of projectiles were examined: a spherical projectile and an elongated cylindrical projectile with a hemispherical head.

2. Validation results

2.1. Aluminum sphere perforating a stationary thin aluminum plate

To further check the numerical procedure beyond the comparison mentioned above with Piekutowsky and Poormon experimental data [10] at close to 10km/s, we present results of simulations of normal perforation of thin aluminum plates. The type of analysis, assembly, material models and parameters and boundary conditions are detailed in Appendix A. The thicknesses of the plates were: T_t = 3 and 4 mm. The diameter of the spheres was 10 mm. Five normal impact velocities for the spheres were modeled: 5, 7.5, 10, 12,5 and 15 km/s. All together 20 runs were made.

The resulting hole diameters are compared to results of an empirical model [18] which is based on 859 data sets of experimental results for projectile diameters of 1.6 – 19.0 mm, target thicknesses 0.02 – 9.52 mm and projectile velocity of 0.5 – 12.0 km/s. The materials used there were: 1100-O, 2017-T4, 2024-T3, 6061-T6 and 7075-T5 aluminum alloys. In addition, a direct comparison was made to an example from one set of experimental data [10]

A specific case where the target has T_t = 4 mm, impacted by a 10mm sphere moving at 10 km/s is shown in Fig. 2. A transparent top view with von Mises stress distribution is shown in Fig. 2a. Fig. 2b shows the isometric solid cut view. A solid X-Y cut view at the center of the target is shown in Fig. 2c. The hole is not smooth and there are protruding "lips" around the cavity as mentioned in [18, 10,21]. Next, we calculate the average crater diameter $D_h = \frac{1}{2}(D_{max} + D_{min})$ where D_{min} is the actual perforation and D_{max} is the partly damaged zone, referred to as “lips” (Fig. 2a). D_{min} in this case is 25 mm and the partly damaged rim's diameter D_{max} =36mm. The mesh size is ~0.5 mm, which means that the accuracy of numerical measurements is within ± 0/5 mm, so that the lip's width is 5.5mm, i.e D_{max} /D_{min} =1.44 ± 0.06 mm. We also see a thickening of the lip area due to the deformations which indicates s a weakening of the lip zone.

The numerical results of the simulations for D_h are summarized in Table 1. The empirical model[18] (Eq. (1)) is used for prediction of hole diameter in aluminum plate by a strike of an aluminum projectile.

$$\frac{D_h}{D_p} = C_1\left(\frac{V}{c}\right)^{p_1}\left(\frac{T_t}{D_p}\right)^{p_2}\cos^{p_3}(\theta) + C_2 \tag{1}$$

Where:

D_h - hole diameterD_p - projectile diameter
T_t _ Target plate thickness
V – impact velocity
c – elastic wave velocity within the aluminum

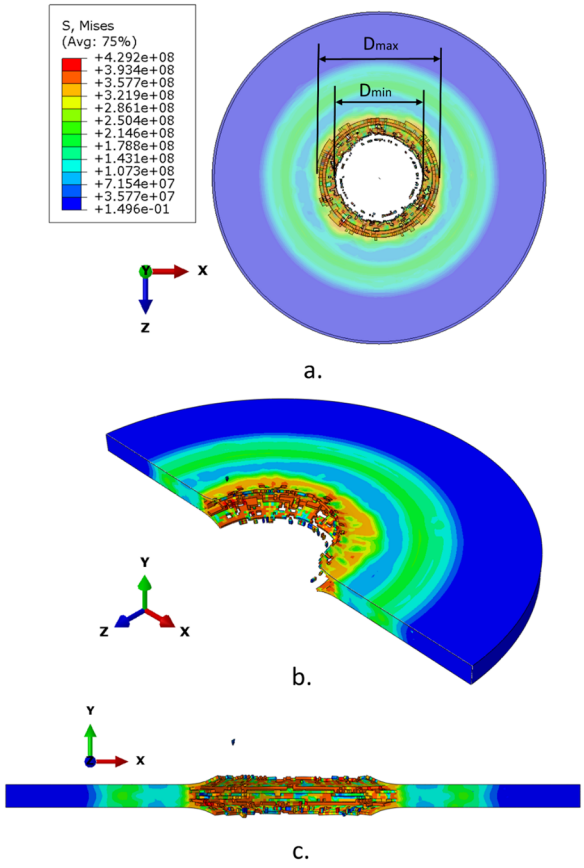

Fig. 2. Perforated plate of Tt=4 mm and impact velocity of 10 km/s. a. Transparent top view. b. Isometric solid cut view. c. A solid X-Y cut view. Note the lips which surround the hole.

Table 1
Calculated average diameters of holes D_h ([mm]) made by a 10mm sphere impacting two target plate thicknesses.

Velocity [km/s]	T_t [mm]	
	3	4
5	23.2	25.2
7.5	25.7	28.4
10	27.3	30.6
12.5	28.8	32.5
15	29.1	33.1

θ - angle of strike (Fig. 1)
C_1, C_2, p_1, p_2 and p_3 – fit parameters

For normal impact θ = 0 and C_1 = 3.20, C_2 = 0.024, p_1 = 0.310, p_2 = 0.355 and p_3 = 0.

The relative difference in percent between the numerical results and the empirical predictions of the model (Eq. (1)) is shown in Fig. 3, calculated by:

$$\left[\left(\frac{D_h}{D_p}\right)^{empirical} - \left(\frac{D_h}{D_p}\right)^{numerical}\right] / \left(\frac{D_h}{D_p}\right)^{empirical} \times 100 \tag{2}$$

The relative difference is less or equal than 12% for the whole range of velocities $5 \le V \le 15$ km/s, which correspond to $0.95 \le \frac{V}{c} \le 2.86$ (Fig 3) where c=5240 m/s (see Appendix A). One has to keep in mind that the empirical model fits only 61.2% of the experimental data sets with a difference less than 5% while 93% are represented with a difference less than 8.8%, and for 7% of the 859 data sets it has a difference of 15% - 71%. Since Eq. (1) is fitted for 5 materials, of which

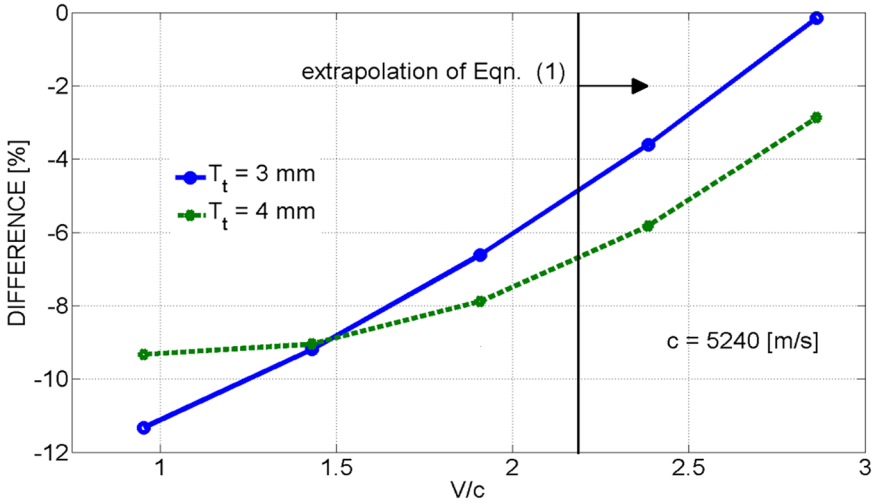

Fig. 3. Difference between calculated and the predicted hole diameters according to Eq. 1. Note that the markers represent the difference from the values of Table 1.

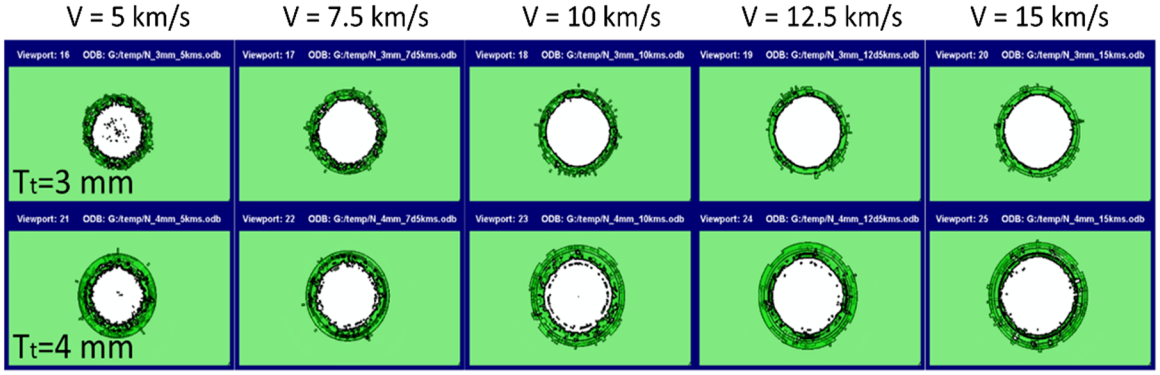

Fig. 4. Transparent normal view of the perforation holes.

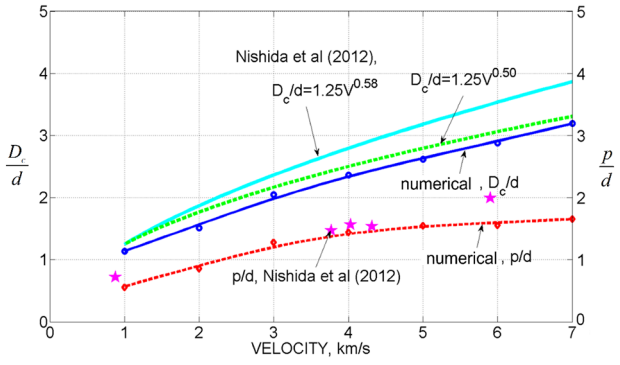

Fig. 5. Comparison of the normalized numerical depths and diameters of the craters due to impact velocity in the range 0.5 – 7 km/s to the experimental results of Nishida et al. [20]. The stars (pink) represent experimental normalized depth results while the red dash line with diamond markers are the numerical results for the normalized depth. The dotted green line and the solid cyan line represent experimental results for the normalized diameter of the crater while the solid blue line with circle markers represent the numerical results for the normalized crater's diameter.

one is modelled here, Fig. 3 can be seen to represent a satisfactory agreement between experiments and simulations. Moreover, the experimental data sets involve a range of impact velocities $0.1 \leq \frac{V}{c} \leq 2.22$. Calculated results for impact velocities exceeding 11.6 km/s are therefore compared with an extrapolation of Eq. (1). Since our results show the same trends as the empirical ones and within less than 2% for a specific case, we conclude that the agreement of the numerical results to known experimental results is satisfactory.

Transparent normal views of the holes of all the runs are shown in Fig. 4, all at the same scale. We see that the hole diameter increases both with the plate thickness and impact velocity. The lips are wider for thicker plates. This can be explained by the fact that the thicker plate absorbs more of the impactor energy during the transient penetration process.

2.2. Aluminum sphere penetrating a stationary thick aluminum target

We now simulate the impact of a sphere on a thick plate and compare our results to experimental results [19,20]. The plate thickness was $T_t = 40$ mm, and the diameter of the sphere was changed to D = 6.35 mm [19].

The type of analysis, material models and parameters and boundary conditions are detailed in Appendix A. The assembly and mesh are given in Appendix B.

Nishida et al. [20] investigated the effects of projectile material properties on crater shape and ejecta in thick aluminum alloy 6061-T6 targets at velocities ranging from approximately 0.5 to 6 km/s. Four types of projectiles with a diameter of 3.2 mm (1/8 inches) made of pure iron, bearing steel, aluminum alloy (2017-T4) and polycarbonate were used. The targets were made of aluminum alloy 6061-T6 and had a diameter of 95 mm and thickness of 20 mm or 30 mm (depending on the impact velocity).

The numerical results of the crater depth (p) and diameter (D_c) for impact velocities 1– 7 km/s are compared in Fig. 5. The results are normalized by the diameter of the sphere (d). The normalized numerical depths are marked by red circles and fitted by a solid red line. A

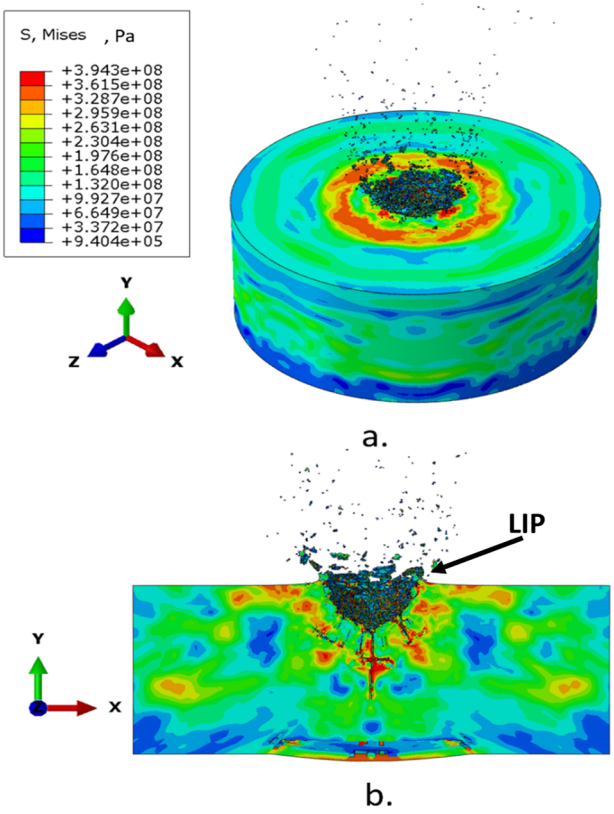

Fig. 6. . The damaged target due to impact at 7 km/s after 25 μs with Mises stress distribution. a. Isometric view. b. A cut view which expose the crater dimensions. The time elapsed (t = 25 μs) is sufficient to encompass the entire event Note the formation of lips around the cavity, as in experimental observations [22].

fairly good agreement with the experimental results of [20] is obtained.

The normalized diameters of the craters are marked by blue circles and fitted by a solid blue line. It can be observed that the crater diameter increased with increasing impact velocity. The crater diameter is usually fitted by a power function of the impact velocity (V): $\frac{D_c}{d} = aV^m$. Nishida et al [20] suggested the values: a = 1.25 and m = 0.58. Their results are plotted as a solid cyan line. We could fit our numerical results with m = 0.5 as shown by the dashed green line. The experimental values of m for pure iron spheres and polycarbonate spheres were close to 0.75 and 0.5 respectively in [20].

Results for impact velocity of 7 km/s are shown in Fig. 6. An isometric view with von Mises stress distribution is shown in Fig. 6a. A cut view which exposes the crater size is shown in Fig. 6b.

The results [19] of the evolution of the crater depth and diameter due to impact of a 6.35 mm diameter Al 2017 spherical projectile impacting at velocity of 7 km/s on a 6061-T6 target were compared to our numerical results. (The comparison is detailed in the supplemental material).The numerical normalized depths and diameters evolutions are 15-20% lower than the experimental results for 6061-T6.

The numerical results show that the initial penetration phase (first ~1.5 μs) involves very high pressures (~250 GPa) which can cause melting, [23], who refer to pressure values of 250 GPa and more. Yet, the very short duration of possible local very high pressure, which could at best lead to limited melting will most probably not alter the general accuracy and relevance of the results reported herein. Yet, enhancing the material models to include phase transformations and improving the EOS may enhance the accuracy (especially at the early penetration phase) of the simulations, albeit at the cost of heavy complications in the calculations, which induce additional approximations.

3. Hypervelocity glancing collisions: results and discussion

3.1. Comparison between glancing and normal impact – spherical projectiles

As an example of the differences in craters due to normal and glancing impacts we simulate penetration into a thick aluminum plate moving at a velocity of 10 km/s perpendicularly to the projectile motion.

The penetration is achieved by normal impact of spherical aluminum projectiles. Both the target plate and the impacting sphere travel at hypervelocity speeds. The problem is similar to the one presented in Section 2.2 with one major difference: the target is no longer

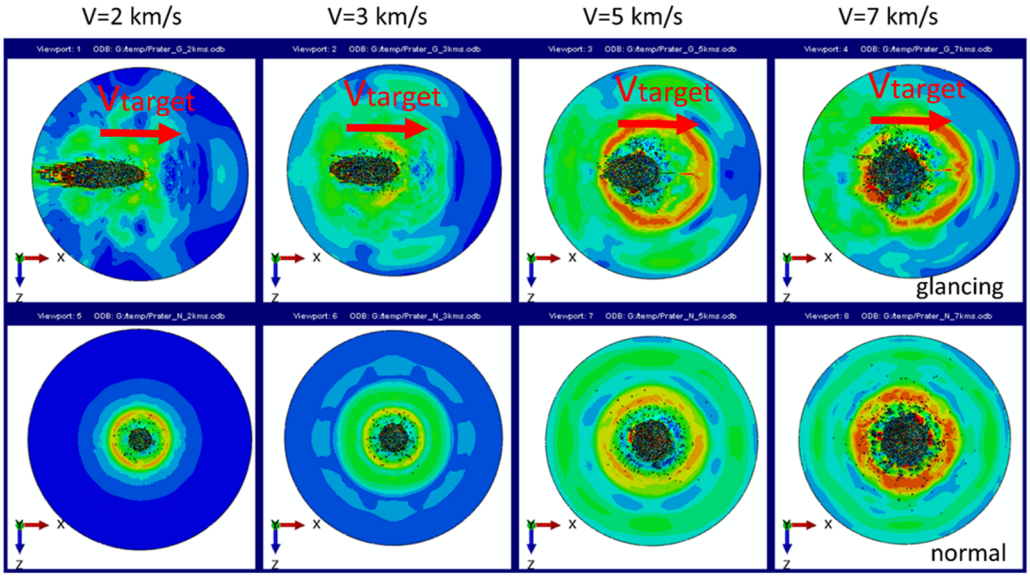

Fig. 7. Solid top views for normal impact velocities of 2, 3, 5 and 7 km/s. The top row presents results due to glancing collisions for initial target speed of 10 km/s. The bottom row presents results due to normal collision on a stationary target for the same impactor velocities. The color map represents the Mises stress distribution.

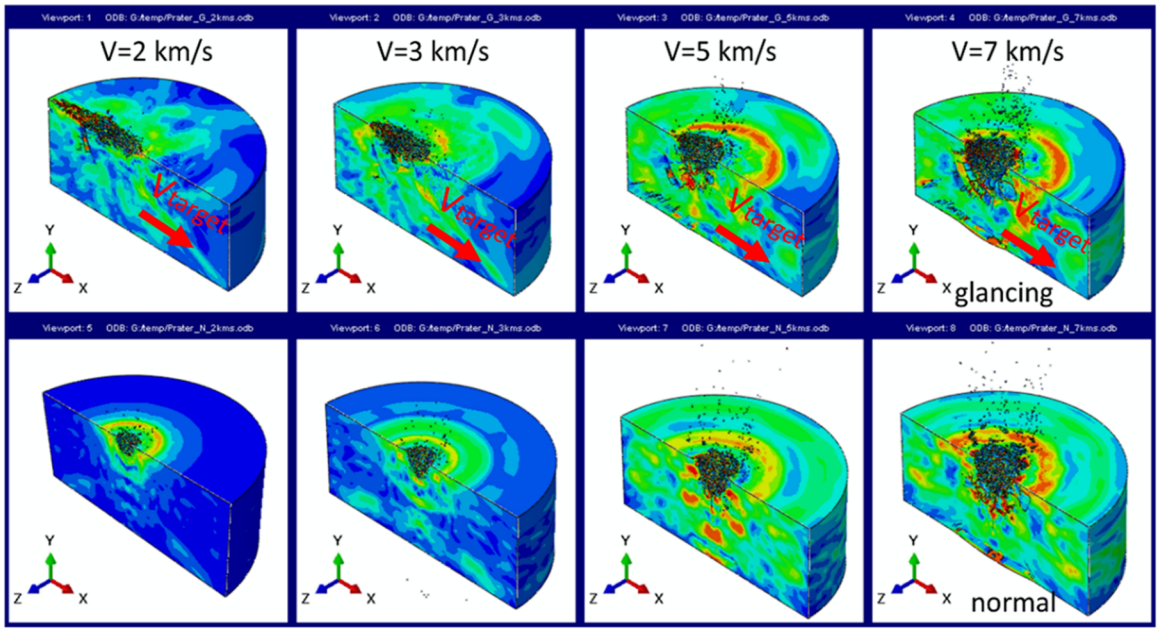

Fig. 8. Isometric cut views for normal impact velocities of 2, 3, 5 and 7 km/s. The top row presents results due to glancing collisions for initial target speed of 10 km/s. The bottom row presents results for a nonmoving target. The color map represents Mises stress distribution.

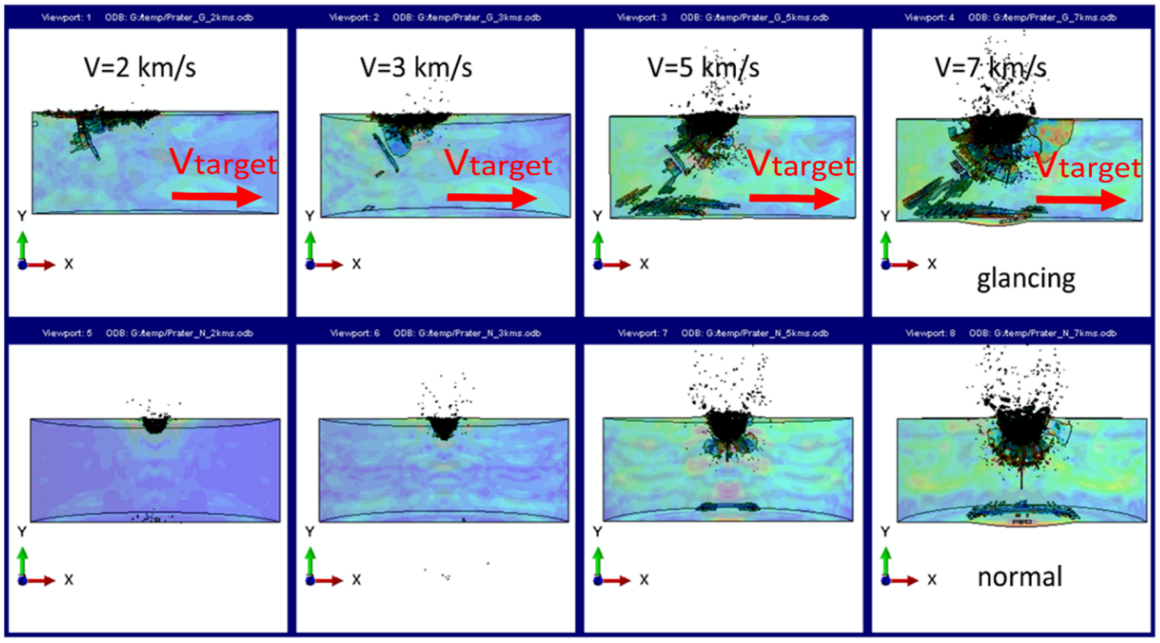

Fig. 9. Transparent cut views for normal impact velocities of 2, 3, 5 and 7 km/s. The top row presents results due to glancing collisions for initial target speed of 10 km/s. The bottom row presents results due to stationary collision. The color map represents Mises stress distribution.

Table 2.
The failed volume due to oblique and glancing collision at different θ angles – spherical projectile.

VOLUME [cm^3] oblique	glancing	θ^o
0.97	0.93	11.3
3.27	3.70	26.6
6.69	6.57	35.0
8.19	8.25	45.0

stationary but moves in the X direction at hypervelocity speed (the coordinate system is shown in Figs. 1 and 2).

A comparison between normal and glancing collision is shown in Figs. 8-10 for 4 normal impact velocities: 2, 3, 5 and 7 km/s. The comparison is done at 25 μs after first contact between the sphere and the plate. Mises stress color maps are shown on Figs. 7-9. The columns in Figs. 7-9 represent normal impact velocities where the 1st left column is for v = 2 km/s and the 4th column on the right is for v = 7 km/s. The top row shows the damage due to the glancing collision while the bottom row shows that due to normal collision.

Solid top views are shown in Fig. 7. Solid cut isometric views are

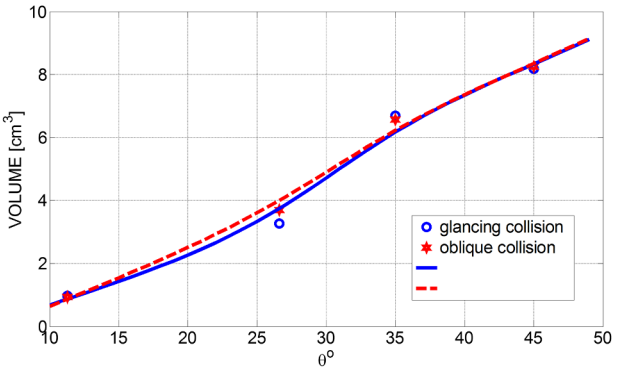

Fig. 10. The failed volume due to oblique and glancing collision at different θ angles.

shown in Fig. 8. The cut is done at Z = 0 and exposes the trajectory of the sphere and its location on the target. A transparent cut view at Z = 0 is shown in Fig. 9 which exposes the trajectory and the damage.

Figs. 7–9 show that the cavity due to glancing collision is very different from that created by a normal collision for all the tested normal impact velocities, as expected. The crater and damage due to the glancing collision are no longer axisymmetric, the crater becomes elongated and shallower while the cracking damage appear mostly at the lower left side (-X direction). As the ratio between the impactor velocity and the target velocity decreases, the cavity becomes shallower and more elongated along the target speed direction.

As the target velocity grows, especially when larger than the impactor velocity the depth of penetration decreases. Obviously, the effect is more pronounced when the target is thicker than that of the impactor dimension in its direction of motion (the diameter for our spherical striker). This is because the penetration process for thin plates is so short that the target motion has less effect.

3.2. Comparison between glancing and oblique impact – spherical projectiles

A comparison of the damage caused to the thick target plate by

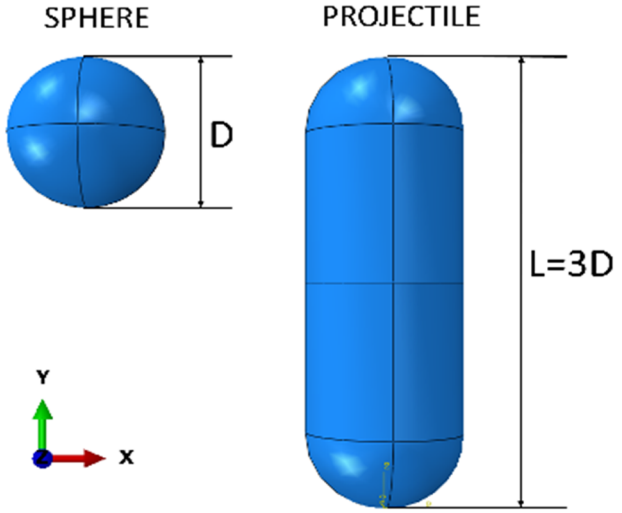

Fig. 12. The elongated projectile geometry in comparison to the spherical projectile.

oblique and glancing hypervelocity collisions is studied next. In the oblique collision the lateral velocity of the target was added to the projectile in the opposite direction as shown in Fig. 1. Four cases were tested, differing by the angle θ which is defined by: $\theta = \text{atan}(\frac{V_{vertical}}{V_{lateral}})$ the angle of inclination from the lateral direction. The four cases were θ = 11.3°, 26.6°, 35°and 45°. The lateral velocity was kept 10 km/s in all these four cases. The failed elements volume was monitored with the aid of the STATUS variable [24] of Abaqus. (failed elements can be found in both the plate and sphere. We are interested in the failed elements of the target only, hence the non-active elements of the sphere are not accounted for. The remaining failed volume of the target is monitored by using the QUERY option of Abaqus [24]

The results of the failed target volume in [cm^3] is given in Table 2 and plotted in Fig. 10. The markers in Fig. 10 represent the values of Table 2 while the lines are smoothing splines of the data.

It can be observed in Fig. 10 that the damaged volume is very

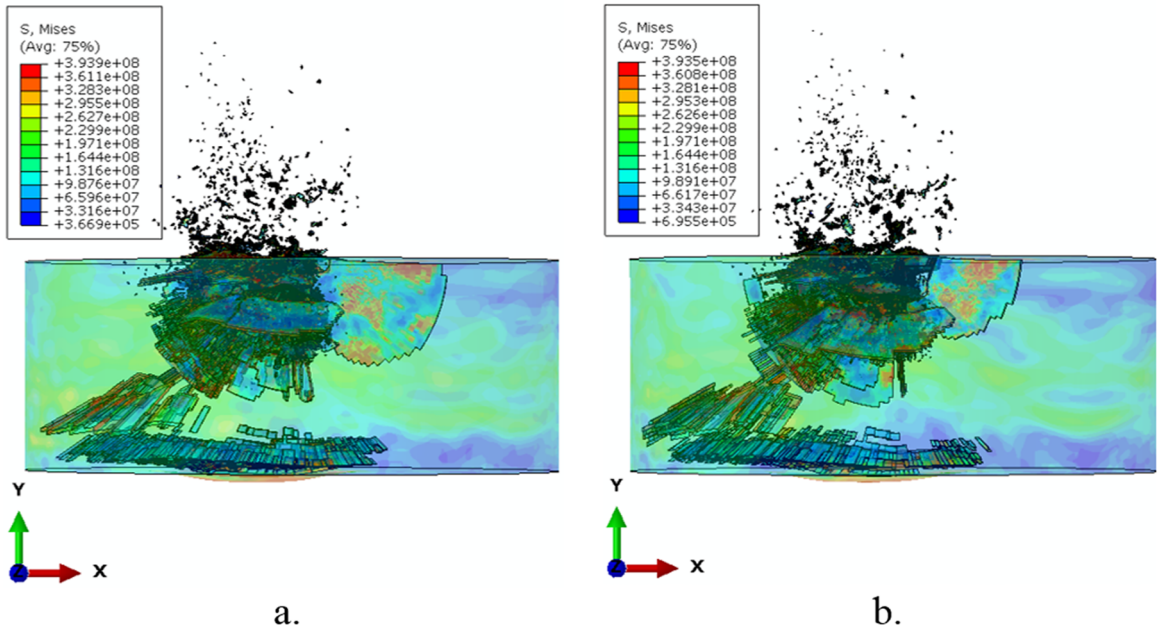

Fig. 11. Transparent cut view of the target at t = 25 μs after impact for θ = 45°. a. Glancing collision. b. Oblique collision. Note the similarity of the damage shape and size.

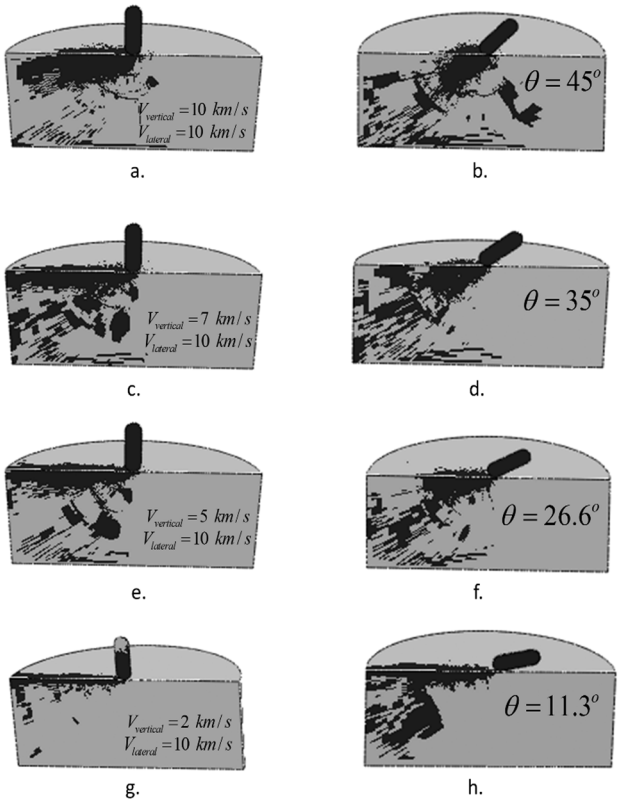

Fig. 13. The undeformed targets due to glancing (left) and oblique(right) impacts at θ = 11.3˚, 26.6˚, 35˚ 45˚ and $V_{lateral} = 10\ km/s$. The failed elements are in black. a,b. θ = 45˚, $V_{vertical} = 10\ km/s$. c,d. θ = 35˚, $V_{vertical} = 7\ km/s$. d,e. θ = 22.6˚, $V_{vertical} = 5\ km/s$. f,g. θ = 11.3˚, $V_{vertical} = 2\ km/s$.

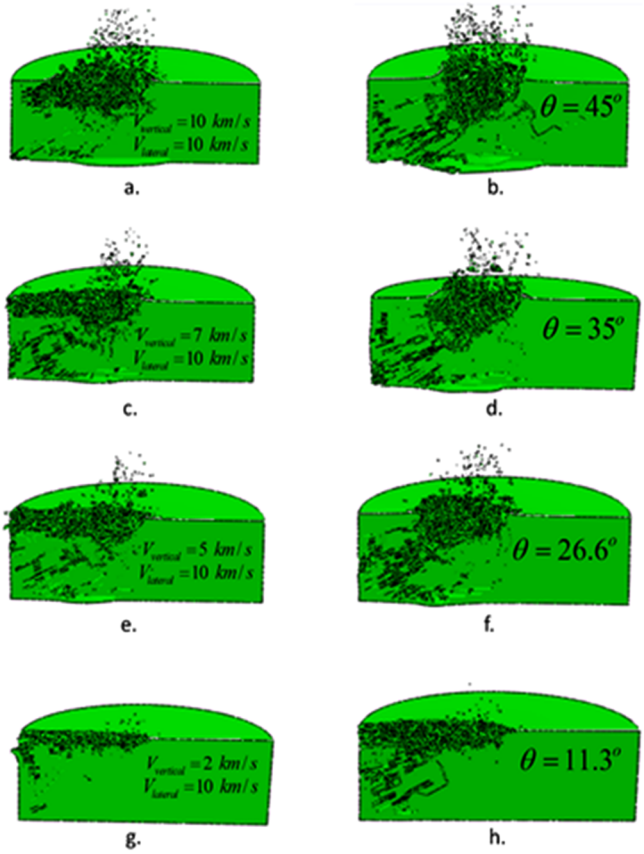

Fig. 14. The deformed targets due to glancing (left) and oblique (right) impacts at θ = 11.3˚, 26.6˚, 35˚, 45˚ and $V_{lateral} = 10\ km/s$. The failed elements are removed. a,b. θ = 45˚, $V_{vertical} = 10\ km/s$. c,d. θ = 35˚, $V_{vertical} = 7\ km/s$. d,e. θ = 22.6˚, $V_{vertical} = 5\ km/s$. f,g. θ = 11.3˚, $V_{vertical} = 2\ km/s$.

similar for both types of collisions at all $11.3^\circ \le \theta \le 45^\circ$.

A transparent cut-view of the targets is shown in Fig. 11 for θ = 45˚. The damage size and shape for both types of impact are also very similar. It can be concluded from Figs. 10 and 11 that oblique experiments *with spherical projectiles* can replace glancing experiments in thick targets. In this case, $\frac{D_s}{T} = \frac{6.35}{40} = 0.16$ where D_s is the sphere diameter and T is the target thickness.

3.3. Comparison between glancing and oblique impact – Non-spherical projectile

The effects of glancing impact is much more significant when the impactor is elongated, as the "feeding" of fresh material is asymmetric for glancing [25], but only appears when the time between first contact and full immersion of the impactor is longer, so that the target has time to move. The projectile chosen has the same diameter of the previous sphere, but its length is three times the diameter: L = 3D. The projectile in comparison to the sphere is shown in Fig 12.

The difference in the impact types is shown in Fig. 1. It is assumed that the projectile hits the target at an inclination angle θ as shown in Fig. 1c. The applied initial velocities are also shown in Fig 1c. A comparison between the damaged zones is shown in Figs. 13 and 14 for θ = 11.3˚, 26.6˚, 35˚ 45˚ and$V_{lateral} = 10$ km/s. The status value on the undeformed targets is shown in Fig. 13 where the failed elements are painted black. The deformed targets, without the failed elements which were removed, are shown in Fig 14. The results for glancing impact are on the left while the corresponding oblique impact are on the right. The craters and the cracking pattern are *completely different* for the two types of collisions for all angles of inclinations.

The glancing impact damage patterns are shallower but have elongated with less cracking in comparison to the oblique collision.

Table 3.
The failed volume due to oblique and glancing collision at different θ angles – non spherical projectile.

VOLUME [cm^3] oblique	glancing	θ^o
8.9	3.3	11.3
17.7	16.5	26.6
18.7	15.6	35.0
24.8	18.7	45.0

The volume of the target's failed elements of Figs. 13 and 14 appears in Table 3. It is interesting to note that the oblique impact results in higher failed volume for all the inclination angles.

4. Conclusion

- Normal and glancing collisions result in highly different craters and damage patterns (for the same normal impact velocity) for relatively thick targets.
- The crater and damage due to the glancing collision are no longer axisymmetric, becoming elongated and shallower while the cracking damage appears mostly beneath and away from the impact location, opposite to the target's direction of motion.
- The ratio between the normal impact velocity and the target velocity has a large effect on the crater and damage. The lower the ratio, the shallower the crater's depth and the larger its elongation opposite to the direction of the target motion.
- Oblique and glancing collisions of spherical projectiles result in similar craters and damage patterns (for the same normal impact

velocity) for relatively thick targets.
- Oblique and glancing collisions of elongated projectiles on relatively thick targets (relative to the projectile diameter) result in vastly different craters and damage patterns (for the same normal impact velocity).

Declaration of Competing Interest

The authors declare that they have no known competing financial interests or personal relationships that could have appeared to influence the work reported in this paper.

Acknowledgements

The authors would like to thank Dr. Andrew Piekutowski for kindly supplying us with supplementary information about his published results and discussions, and the Asher Space Research Institute for financial support of this study.

Appendix A

The assembly contains two parts: a sphere and a cylindrical target. (Fig. A1). A normal view is shown on the upper left side with a detail of the spherical projectile on the upper right side. An isometric view is shown on the bottom left side of the figure with a detail on the bottom right side. In the example the diameter of the sphere is d (d = 10 mm in Fig. A1). The diameter of the plate is D = 100 mm so as to and its thickness is T_t (T_t = 4 mm in Fig. A1). T_t and d are varied between runs. At time t = 0 the spherical projectile just touches the center of the upper target surface with an initial hypervelocity normal velocity V. The ambient temperature is taken to be 273K. The target and projectile were described by a mesh with linear hexahedral elements of type C3D8R and linear wedge elements of type C3D6 [24] . The projectile has 12096 elements of type C3D8R and1664 elements of type C3D6. The 4 mm thick target (Fig. 1) has 76416 elements of type C3D8R. The simulation duration was 5 μs.

The simulations are done using the commercial finite element software Abaqus Explicit [16]. A 3D adiabatic, transient and non-linear simulation is conducted. The targets and projectiles consist of aluminum 6061 T6 [17]. The volumetric behavior is described by the Mie-Gruneisen equation of state (EOS) model while the deviatoric behavior is elastic-plastic assuming a linear elastic model with Johnson-Cook plasticity [24]. All surfaces of target and sphere are initially free. The general contact algorithm of Abaqus [24] is used with element-based surfaces which can adapt to the exposed surfaces of the current non-failed elements. Abaqus' frictional tangential behavior with coefficient of friction f = 0.34 [26,27] is adopted. The NODAL EROSION parameter is set to "NO" so contact nodes still take part in the contact calculations even after all of the surrounding elements have failed.

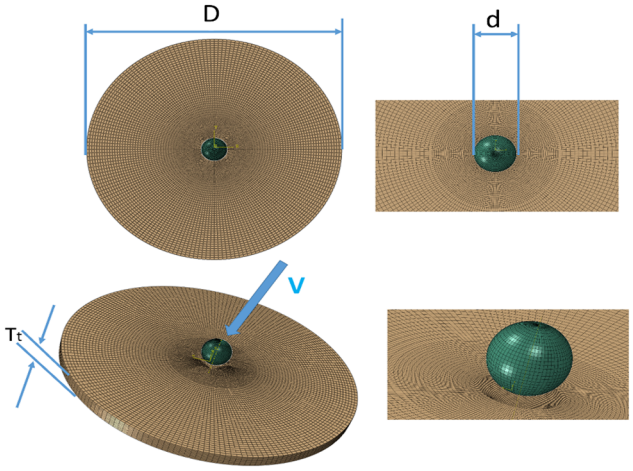

Fig. A1. Normal and isometric view of the meshed assembly.

The parameters used for the Mie-Gruneisen EOS for Aluminum 6061-T6 are: Gruneisen coefficient, $\Gamma_{0,}$ = 1.97, Wave speed, c_0 = 5240 m/s and parameter s = 1.4.

The parameters for the Johnson-Cook (JC) material model and the Johnson-Cook dynamic failure are taken from ref [17]. Table A1 summarizes the physical properties. The value of inelastic heat fraction was taken to be 0.5 [28] (note that Abaqus by default use a value of 1 when EOS is used). Table A2 summarizes the JC material model parameters, and the corresponding failure parameters are summarized in Table A3.

A "tensile failure" spall criterion [24] of 600MPa [30] was added to the conditions. The tensile criterion does not affect the crater dimensions but the plate cracking pattern.

Table A1.
Physical properties for aluminum 6061 T6 [17,29].

Reference density [Kg/m^3]	Shear modulus, G [GPa]	Reference temperature, T_r, [K]	Melting temperature, T_m, [K]	Inelastic heat fraction,β	Specific heat [J/Kg K]
2703	25.94	293	750	0.5	885

Table A2.
The JC dynamic properties for Aluminum 6061 T6 [17,29].

A , [MPa]	B , [MPa]	n	m	C	$\dot{\varepsilon}_0$
324.1	113.8	0.42	1.34	0.002	1

Table A3.
The JC dynamic failure properties for Aluminum 6061 T6 [17,29].

d_1	d_2	d_3	d_4	d_5
-0.77	1.45	0.47	0	1.6

Appendix B

The meshed assembly is shown in Fig. B1a. An exposed detail of the mesh at the impact location is shown in Fig. B1b. The mesh of the sphere has 13760 elements where 12224 are linear hexahedral elements of type C3D8R and 1536 are linear wedge elements of type C3D6. The mesh of the target is made of 2,337,608 linear hexahedral elements of type C3D8R, The size of the target mesh near the impact location is ~0.168 mm. The mesh was made fine to be able to accurately measure the crater diameter and depth.

Seven simulations which correspond to impact velocities of 1, 2, 3, 4, 5, 6, and 7 km/s were performed

The damaged target at t = 25 μs, which is time enough to encompass the total event.

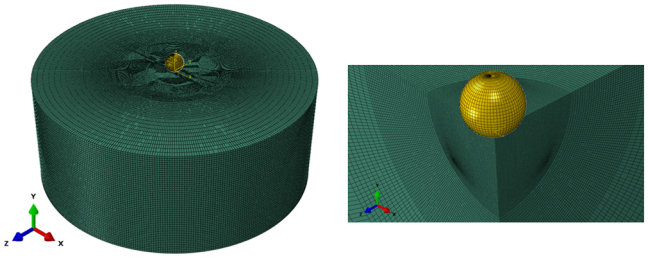

a. b.

Fig. B1. a. The meshed assembly. b. A detail showing the mesh at the vicinity of impact location.

Appendix C Validation of the computation by comparison to experimental data

As mentioned in the main text, we validated the high speed (10 km/s) calculations, which are at the limits of the material properties EOS by comparison to experimental data from the literature [10] and consultation with the senior author of the data, Dr Andrew Piekutowski.

The table below shows the results of these comparisons, showing that the material model and EOS we used are valid for such collision speeds.

The first two cases are for thin plates (<3 mm) while the third is for a thicker plate of about 4 mm. In thicker plates the hole is no longer exactly round, as mentioned by the authors, and Dr Piekutowski in a personal communication. This means that the measurement of the diameter ratio is no longer as accurate, as both the experiments, and our calculations show.

Quoting Dr Piekutowski:

"When the *t/D* ratio was greater than 0.3, evolution of the hole becomes more complex as the expanding ring is formed and may or may not remain in the hole after the event is over… Holes formed in the thicker sheets are seldom as round as the holes formed in thinner sheets and their surfaces tend to be jagged, so any measurements of their diameters tend to be subjective at best"

Table C1.
The shot numbers are taken from Ref. [10]. t is plate thickness D_h is hole diameter, D_p is projectile (sphere) diameter.

Shot No.	Impact Velocity [m/s]	Sphere diameter [mm]	$\frac{t}{D_p}$	Experimental $(\frac{D_h}{D_p})_{\exp}$	Numerical $(\frac{D_h}{D_p})_{num}$	Difference [%]
8-3326	9680	1.50	0.209	2.133	2.23	4.6
8-3302	9790	1.44	0.230	2.254	2.12	5.9
8-3275	9400	1.60	0.374	2.767	2.98	7.7

References

[1] Cour-Palais BG. Hypervelocity impact in metals, glass and composites. Int J Impact Eng 1987;5:221–37. https://doi.org/10.1016/0734-743X(87)90040-6.

[2] Bernhard RP, Christiansen EL, Kerr JH. Space shuttle meteoroid and orbital debris impact damage. Int J Impact Eng 2001;26:33–8. https://doi.org/10.1016/S0734-743X(01)00073-2.

[3] Mandeville J-C, Perrin J-M, Vidal L. Experimental hypervelocity impacts: implication for the analysis of material retrieved after exposure to space environment: Part I. Impacts on aluminium targets. Acta Astronaut 2012;81:532–44. https://doi.org/10.1016/J.ACTAASTRO.2012.08.033.

[4] Valerio-Flores OL, Murr LE, Hernandez VS, Quinones SA. Observations and simulations of the low velocity-to-hypervelocity impact crater transition for a range of

penetrator densities into thick aluminum targets. J Mater Sci 2004;39:6271–89. https://doi.org/10.1023/B:JMSC.0000043597.72588.d1.
[5] Mespoulet J, Héreil P-L, Abdulhamid H, Deconinck P, Puillet C. Experimental study of hypervelocity impacts on space shields above 8 km/s. Procedia Eng 2017;204:508–15. https://doi.org/10.1016/J.PROENG.2017.09.748.
[6] Piekutowski AJ, Poormon KL. Effects of Scale on the Performance of Whipple Shields for Impact Velocities Ranging from 7 to 10 km/s. Procedia Eng 2013;58:642–52.
[7] Christiansen EL. Design and performance equations for advanced meteoroid and debris shields. Int J Impact Eng 1993;14(1-4):145–56. https://doi.org/10.1016/0734-743X(93)90016-Z.
[8] Gongshun G, Baojun P, Wei Z, Yue H. Crater distribution on the rear wall of AL-Whipple shield by hypervelocity impacts of AL-spheres. Int J Impact Eng 2008;35:1541–6. https://doi.org/10.1016/J.IJIMPENG.2008.07.028.
[9] Dhote KD, Verma PN. Investigation of hole size formation by steel sphere impacting on thin plate at hypervelocity. Procedia Eng 2017;173:323–30. https://doi.org/10.1016/J.PROENG.2016.12.025.
[10] Piekutowski AJ, Poormon KL. Holes Formed in Thin Aluminum Sheets by Spheres with Impact Velocities Ranging from 2 to 10 Km/S. Procedia Eng 2015;103:482–9. https://doi.org/10.1016/J.PROENG.2015.04.063.
[11] Schonberg WP, Taylor RA. Penetration and ricochet phenomena in oblique hypervelocity impact. AIAA J 1989;27:639–46. https://doi.org/10.2514/3.10155.
[12] Burchell MJ, Grey IDS. Oblique hypervelocity impacts on thick glass targets. Mater Sci Eng A 2001;303:134–41. https://doi.org/10.1016/S0921-5093(00)01847-5.
[13] Rosenberg Z, Kositski R. The hole diameter in metallic plates impacted by hypervelocity projectiles. Int J Impact Eng 2017;102:147–55. https://doi.org/10.1016/J.IJIMPENG.2016.12.015.
[14] Francesconi A, Giacomuzzo C, Olivieri L, Sarego G, Duzzi M, Feltrin F, et al. CST: A new semi-empirical tool for simulating spacecraft collisions in orbit. Acta Astronaut 2019;160:195–205. https://doi.org/10.1016/j.actaastro.2019.04.035.
[15] Frankel I, Weihs D. Hydrodynamic theory of glancing impact. J Fluid Mech 1990;216:213–29. https://doi.org/10.1017/S0022112090000404.
[16] Simulia. Abaqus/CAE version 6.14-2 (2014). Providence, RI, USA: Dassault Systèmes Simulia Corp.; 2014.
[17] Abaqus Technology Brief DS.Simulation of the ballistic perforation of aluminium plates with Abaqus/Explicit. 2012.
[18] Hatami H, Hosseini M, Karimdoost Yasuri A. Perforation of thin aluminum targets under hypervelocity impact of aluminum spherical projectiles. Mater Eval 2019;77(3):411–22.
[19] Prater, R. F. Mjr., USAF.: Hypervelocity impact-material strength effects on crater formation and shock propagation in three aluminum alloys. 1970 .AFMLTR-70-295, Air Force Systems Command, Wright-Patterson AFB, Ohio.
[20] Nishida M, Yamamoto S, Hayashi K, Hasegawa S. Influence of projectile material properties on crater size and ejecta of thick aluminum alloy 6061-T6 targets in hypervelocity impact. J Jpn Soc Exp Mech 2012;12(Special_Issue):s163–9.
[21] Piekutowski AJ. Holes produced in thin aluminum sheets by the hypervelocity impact of aluminum spheres. Int J Impact Eng 1999;23:711–22. https://doi.org/10.1016/S0734-743X(99)00116-5.
[22] Piekutowski A. Cratering mechanisms observed in laboratory-scale high explosive experiments. In: Roddy DJ, Pepin RO, Merrill RB, editors. Impact and explosion cratering. 1977. p. 67–102.
[23] de Rességuier T, Loison D, Dragon A, Lescoute E. Laser driven compression to investigate shock-induced melting of metals. Metals (Basel) 2014;4:490–502. https://doi.org/10.3390/met4040490.
[24] Simulia. Abaqus/Explicit Version 6.14-2. Abaqus documentation . Dassault systemes; 2014. p. 2014.
[25] Jia X, Huang Z, Xu M, Xiao Q, Liu X, Zhang X, et al. Study on interaction mechanism between the shaped charge jet and thick moving target. Propellants, Explos Pyrotech 2019;44:1033–48. https://doi.org/10.1002/prep.201800248.
[26] Espinosa H.D., Patanella A.J., Fischer M.Dynamic friction measurements at sliding velocities representative of high-speed machining processes. 2000.
[27] Tomimura T, Ikeda T, Hirasawa S. Effective dynamic coefficient of friction between rotating rod and aluminum alloy plate evaluated by thermal method. Q J Jpn Welding Soc 2009;27(2):104s–8s.
[28] Rittel D, Zhang LH, Osovski S. The dependence of the Taylor–Quinney coefficient on the dynamic loading mode. J Mech Phys Solids 2017;107:96–114. https://doi.org/10.1016/J.JMPS.2017.06.016.
[29] Silnikov MV, Guk IV, Nechunaev AF, Smirnov NN. Numerical simulation of hypervelocity impact problem for spacecraft shielding elements. Acta Astronaut 2018;150:56–62. https://doi.org/10.1016/J.ACTAASTRO.2017.08.030.
[30] Cohen L, Berkowitz H. Time-dependent fracture criteria for 6061-T6 aluminum under stress-wave loading in uniaxial strain. Int J Fract Mech 1971;7:183–96. https://doi.org/10.1007/BF00183805.